This article has been accepted for publication in a future issue of this journal, but has not been fully edited. Content may change prior to final publication. Citation information: DOI 10.1109/TMECH.2020.3037291, IEEE/ASME Transactions on Mechatronics

Structural Failure Detection Using Wireless Transmission Rate from Piezoelectric Energy Harvesters

Hyun Jun Jung, Amin Toghi Eshghi, and Soobum Lee

Abstract—**This paper presents a new self-powered wireless failure detection method that uses different signal transmission rates from piezoelectric energy harvesters. Reliable signal transmission from a wireless sensor network has been challenging due to the power supply issue, often covered by batteries that need regular replacement. Piezoelectric energy harvesting is an excellent option to power the sensors in a vibrational environment, but the power level is limited by input vibrational energy. In this paper, we introduce a new failure detection strategy that uses multifunctional piezoelectric material for vibration sensing and energy harvesting. That is, when the vibration is stronger and the material strain is higher, piezoelectric material produces higher voltage and power. Different power level from multiple piezoelectric sensors is used for sensing structural failure. We design a simple power management circuit that saves power proportional to the piezoelectric voltage so that the piezoelectric patch with higher strain can transmit more frequent wireless signals (higher transmission rate). To store the piezoelectric power, the circuit is composed of a full-bridge rectifier, a Single Pole Double Throw (SPDT) switch, a comparator with hysteresis, and a wireless transmitter (Zigbee). The failure detection performance is investigated in a case study that monitors screw joint failure in a vibrating plate. Reliability-based design optimization is conducted to determine the piezoelectric sensor network in terms of the number and sizes of multiple piezoelectric (PZT) patches. The test results show that the proposed system successfully powers the wireless transmitter using the ultra-low scale of power from the PZT sensors (microwatt) and detect the different combination of screw joint failure in the vibrating plate.**

Index Terms— **Piezoelectric sensor, wireless transmitter, transmission rate, reliability-based design optimization**

I. INTRODUCTION

A low cost but reliable monitoring system is necessary to ensure safe and functional mechanical structures. Usually, this sensing technology requires a large number of distributed sensors to perform the required monitoring process. Moreover, various uncertainty from structure properties, external loading, and environmental condition changes adversely affects the reliability of SHM sensors. One important aspect of smart sensing is to overcome these shortcomings (cost, reliability) by determining the optimum number and placement of the sensors on the structure. Piezoelectric materials (e.g. PZT) have attracted considerable attention for structural health monitoring (SHM) techniques [1-3]. Several studies have proposed different methodologies for determining the optimal location of PZT sensors. A thorough review of optimization criteria for placement of PZT sensors for structure monitoring is reported by Gupta et al. [4] and Singhal et al. [5] that introduce methods of maximizing different objectives such as modal forces, deflection of the host structure, dissipated energy, degree of controllability, and degree of observability. Lee et al. [6] searched for optimal sensor locations by maximizing the dissipation energy from the feedback control system using a quasi-Newtonian algorithm. Cha et al. [7] proposed a multi-objective genetic algorithm (MOGA) for optimal sensor placement (OSP). This method is an integration of an implicit redundant representation of the genetic algorithm with the Pareto evolutionary algorithm. It was shown that the proposed algorithm is effective to develop optimal Pareto front curves for optimal placement of sensors. Chhabra et al. [8] considered the optimal placement of PZT sensors on thin plates by using a modified control matrix and singular value decomposition (MCSVD) approach. Only a few studies have been focused on incorporating the uncertainties associated with structures into the numerical simulation for OSP problems. Guratzsch and Mahadevan [9] developed a probabilistic finite element analysis model to obtain sensor output for all possible locations. Castro-Triguero et al. [10] examined the effect of parametric uncertainties on the OSP for modal analysis of a truss bridge. Based on their conclusion the parametric uncertainties have a significant influence on the optimal sensor location. Vincenzi and Simonini [11] considered the effect of both parametric and model uncertainties for OSP where they applied Information Entropy theory to find the optimum solution based on the covariance matrix of prediction error. Wang et al. [12] introduced a new probabilistic technique for OSP by detectability measure. Detectability means the ability of a sensor network that distinguishes different health condition, formulated using Mahalanobis Distance (MD). A practical solution is demonstrated to overcome the computational burdens via surrogate modeling that approximates the stochastic performance of the system.

Powering a wireless SHM sensor node is another challenging issue when a sensor needs to operate in real-time with substantial power and is remotely placed where no wired power is available, especially in outdoor environment. In general, a modern wireless sensor requires power up to hundreds of milliwatt that last just a few days by a compact battery. For instance, the batteries in an accelerometer monitoring a train pantograph only lasted 20 days [13]. Chebrolu et al. [14] could extend the battery life to 1.5 years for 4 AA batteries but serious activation management (wake up and sleep) is required. Extended battery life reduces the number of replacement, but it is still necessary to replace batteries that is not always possible in many remote applications. Energy harvesting (EH) is an excellent alternative powering solution and various studies have considered piezoelectric energy harvesting (PEH) for wireless sensor network systems [15-18]. But its power generation heavily depends on available vibration energy around it [19-21]. Esu et al. [21] mentioned the possible use of vibration-based PEH for powering the wind turbine monitoring system. Overall, various PEH applications have been demonstrated from multiple studies, but its power generation is limited up to sub milliwatt level [22]. In practice, power generation by PEH is limited further when vibration energy is not always available and it may cause inconsistent transmission duty cycle (or signal transmission frequency) and unreliable monitoring performance.

A more advanced idea of combining the sensing and energy harvesting functionality has been proposed by multiple researchers recently. Lim et al. [23] suggested the use of piezoelectric energy harvesters for wind turbine blade monitoring. Based on the fact that changes in structural strain and energy harvesting performance associated with blade damage result in different timing of the RF pulses, they proposed the monitoring algorithm that uses the timing of binary pulses from the RF transmitters. The application of this study is limited because it required multiple (or triple in the wind turbine blade application) redundancies as a reference signal. Chew et al. [24] implemented a time-multiplexing operation for alternating dynamic strain sensing and energy harvesting functions at different time slots associated with different energy levels. They used the micro-fiber composite (MFC) as a strain sensor and an energy harvester. However, this concept does not provide a continuous monitoring solution because of function switch between harvester and sensor – when MFC is used as a harvester, it cannot send signals.

This study presents a new self-powered wireless failure detection method using different power levels from multiple piezoelectric energy harvesters. We utilize a simple but clear fact that piezoelectric material produces a higher voltage when the vibration is stronger and the material strain is higher [23]. When the piezoelectric material is integrated with a proposed power management circuit and a wireless transmitter, one can detect the vibration level by the wireless transmission rate. This is an indirect measurement strategy where low energy harvesting is still meaningful as an indicator of small vibration. This study is the first experimental research to use multifunctional piezoelectric material for sensor "network" design to detect multiple failure modes. In this study, we performed an optimization study to determine a layout of piezoelectric patches that can detect structural failure with minimum use of material, and experimentally verified the sensing performance. The rest of the paper is organized as follows: Section II presents the concept of the proposed self-powered failure monitoring system. Section III introduces the detectability measure and Section VI explains the simulation model and the design process of the PZT patch sensor network. Section V presents the proposed circuit design for power management and wireless transmission with low power consumption. Section VI presents system integration and demonstrates the experimental study to verify the advantage of the proposed system.

II. CONCEPTUAL DESIGN OF SELF-POWERED MONITORING SYSTEM

The proposed self-powered failure detection system is targeted to monitor mechanical joint failure in a vibrating engineering structure. A rivet joint is one of the popular methods to assemble skin (or plate) structures in many engineering applications such as aerospace structures, civil infrastructures, and vehicles. SHM for such joints is highly required because varied environmental conditions (humidity, temperature) as well as operational conditions (pressure, speed, and loading condition) causes their structural damages (e.g., loosening, detachment). Conventionally, one can deploy multiple vibration sensors to each of the rivet joints to monitor them as shown in Fig. 1. This setup has several disadvantages. First, it requires a substantial number of sensors as many as the number of joints to monitor. Second, vibration data needs to be transmitted with a high transmission rate (several tens of seconds) and high sampling frequency, which results in higher power consumption of wireless transmitters. Third, the wireless sensor node needs a separate power supply either from battery or energy harvester and it makes the overall layout of a wireless sensor node very complex. Herein, we propose a new failure detection strategy that utilizes the multifunctional characteristic of PZT material regarding vibration sensing and energy harvesting. That is, PZT material generates power proportional to the vibration level, and one can indirectly measure the vibration level by the generated power. Minimum use of the sensor material (e.g., number, size) is desired to save the sensor material and maintenance cost. Design optimization can be used to design the PZT sensor network to reduce the PZT sensor material while it maintains satisfactory failure detection performance (top in Fig. 1). In this paper, reliability-based

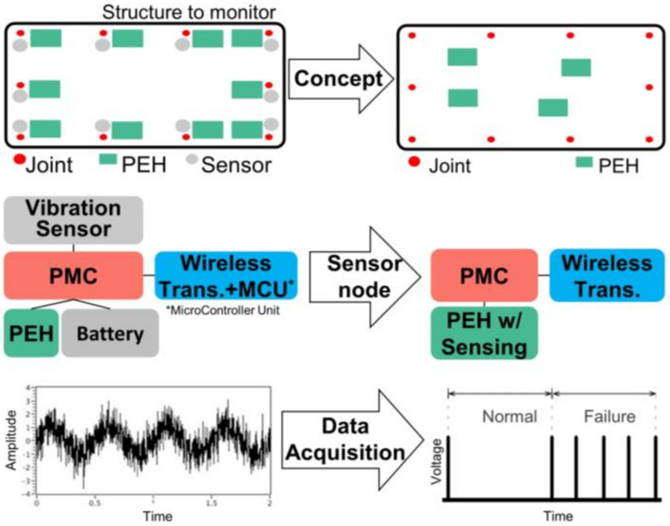

Fig. 1. Concept of proposed self-powered wireless failure detection system.

design optimization (RBDO) is conducted to consider the uncertainty of the system (e.g., structure properties, external loading, and environmental condition changes) in the design process. The design result is prototyped with a new concept of power management circuit (PMC) that consumes minimum power for operation of the wireless transmitter. The PZT materials are used to generate the power for the operation of the wireless transmitter and the power management circuit (PMC). When the PZT material charges a predetermined energy in the PMC capacitor, it powers the transmitter to wirelessly transmit the signal for several milliseconds. If some rivet joints are damaged, the plate vibration pattern becomes different and this changes the power and the wireless transmission rates from the multiple PZT materials. From the change of wireless signal transmission rates, one can detect which joint(s) is failed.

III. QUANTIFICATION OF PROBABILISTIC DETECTABILITY

We first need to define a set of health conditions (HCs). Each HC indicates different failure modes and it can be classified based on the training data on historical operation/failure. The correct detection rate of each health condition is one of the criteria to appraise the probabilistic performance of the sensor network. The correct detection rate can be determined as a conditional probability that the sensor network detects the same HC in which the system is operating at [12, 25]. These detection rates will constitute the probability-of-detection (PoD) matrix, from which the detectability of each HC can be obtained for the sensor network.

A. *Probability-of-detection (PoD) matrix*

A PoD matrix defines the probability of the correct detection for each predefined HC. The general form of the PoD matrix can be shown as [12, 26]:

$$\text{PoD} = \begin{bmatrix} P_{11} & P_{12} & \cdots & P_{1N_{HC}} \\ P_{21} & P_{22} & \cdots & P_{2N_{HC}} \\ \vdots & \vdots & \ddots & \vdots \\ P_{N_{HC}1} & P_{N_{HC}2} & \cdots & P_{N_{HC}N_{HC}} \end{bmatrix} \tag{1}$$

where N_{HC} indicates the total number of classified HCs. P_{ij} is the probability that the system is detected as HC_j by the sensing system given that the system operates at HC_i. In the statistical form P_{ij} can be expressed as:

$$P_{ij} = \Pr(Detected\ as\ HC_j \,|\, Operated\ as\ HC_i) \tag{2}$$

Since any set of data from HC_i will be classified into one of the predefined N_{HC} health conditions, the summation of P_{ij} for j=1 to N_{HC} is equal to unity. In the PoD matrix, the diagonal terms (P_{ii}) will be defined as the detectability (D_i) that determines the probability of correct detection for each predefined HC, or

$$D_i = P_{ii} = \Pr(Detected\ as\ HC_i \,|\, opereted\ as\ HC_i) \tag{3}$$

To design a reliable sensor network, the detectability measured for each HC needs to satisfy the detectability target. The following example explains the detectability measurements. One sensor is used to detect three different HCs. The first HC (HC_1) indicates there is no damage and the sensor data follow a normal distribution as $N(1, 0.8^2)$. The second HC (HC_2) represents some minor damage in the structure and the sensor data follows $N(4, 0.6^2)$. The third HC (HC_3) corresponds to severe damage and the sensor data follows $N(7, 1.4^2)$. Fig. 2 exhibits the PDFs for different HC in this example. Two neutral points ($X_{1\text{-}2}$ and $X_{2\text{-}3}$) can be located where the normalized distances from different distributions are the same, or:

$$\frac{X_{1-2}-1}{0.8} = \frac{4-X_{1-2}}{0.6}, \quad X_{1-2} = 2.7142 \tag{4}$$

$$\frac{X_{2-3}-4}{0.6} = \frac{7-X_{2-3}}{1.4}, \quad X_{2-3} = 4.9000 \tag{5}$$

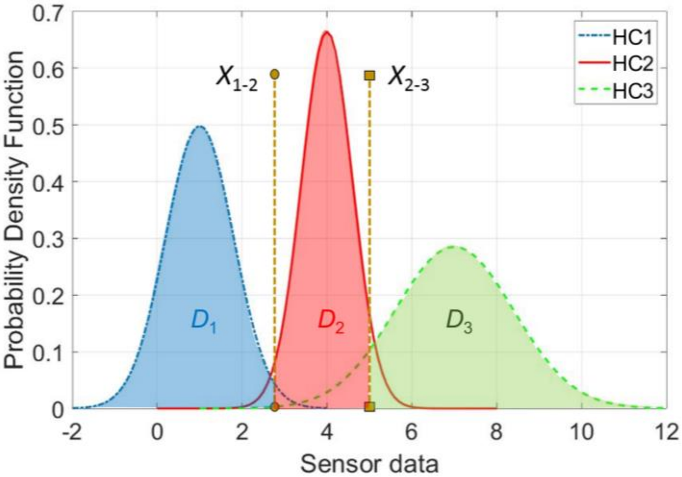

Fig. 2. Sensor output distribution or different HCs and detectability measure.

To obtain the detectability value for each HC we need to classify the sensory data into one of the three HC categories. The classification can be done by evaluating the normalized distances between the testing data and sensor output distribution for each HC. That is, the testing data are classified into each HC of which the normalized distance is smallest. In this one sensor example, this classification can be interpreted as the integration of each PDF bounded by the neutral points as shown in Fig. 2 or:

$$\begin{aligned} D_1 &= P_{11} = \Pr(Detected\ as\ HC_1 \,|\, Operated\ as\ HC_1) \\ &= \Pr(X \le X_{1-2} \,|\, X \sim N(1, 0.8^2)) = 0.9831 \end{aligned} \tag{6}$$

$$\begin{aligned} D_2 &= P_{22} = \Pr(Detected\ as\ HC_2 \,|\, Operated\ as\ HC_2) \\ &= \Pr(X_{1-2} \le X \le X_{2-3} \,|\, X \sim N(4, 0.6^2)) = 0.8959 \end{aligned} \tag{7}$$

$$\begin{aligned} D_3 &= P_{33} = \Pr(Detected\ as\ HC_3 \,|\, Operated\ as\ HC_3) \\ &= \Pr(X \ge X_{2-3} \,|\, X \sim N(7, 1.4^2)) = 0.9331 \end{aligned} \tag{8}$$

In many engineering applications, a sensor network is composed of numerous sensors and HCs where the analytical evaluation of detectability is challenging. Therefore, more complex HC classification methods such as Mahalanobis Distance (MD) [27, 28], linear discriminant analysis [29], or support vector machine [30] is required. Among them, we used a detectability analysis approach using MD due to its capability for classification of a large amount of multivariate data especially when there is a concern of affinities between groups. The next section briefly explains MD hired for classification of the random sensory signals.

B. *Mahalanobis Distance (MD) classifier*

Mahalanobis Distance (MD) measures the distance between online data points and the distribution of the training data sets, and it represents the similarities between the testing data and different training data sets – shorter distance represents greater similarities. That is, a testing data point can be categorized into a HC of which the MD is minimal. To compute MD, we first need to obtain the variance-covariance matrix $\mathbf{C}_x$ for the training data as:

$$\mathbf{C}_x = \frac{1}{(n-1)}(\mathbf{X}\text{-}\bar{\mathbf{X}})^T(\mathbf{X}\text{-}\bar{\mathbf{X}}) \tag{9}$$

where $\mathbf{X}$ is the training data matrix containing n objects in the rows measured for p variables, and $\bar{\mathbf{X}}$ is the matrix of variable means. Consequently, MD can be calculated as:

$$\text{MD}_i = \sqrt{(x_i - \bar{x})\text{C}_x^{-1}(x_i - \bar{x})^T} \tag{10}$$

where x_i is a testing data point to be classified and $\bar{x}$ is the mean of the training data. MD classifier categorizes the testing data sets obtained by a sensing system into a predefined HC.

Consider another example with two sensors and three predefined HCs. The training data for each sensor (TABLE I) consists of a normally distributed random data for different HCs (1,000 sensory data point for each HC). Six different testing data in the first two columns of TABLE II will be classified in one of the HCs, by evaluating MD in equation (10). The distribution of the training data for three different HC is shown in Fig. 3. At each HC, the MD is obtained for the testing data shown in TABLE II. As discussed before, the testing data is classified into a group with the least MD. For instance, to classify the first testing data [3.02 1.45], three different MD values are measured using equation (1) to evaluate similarity to each group of training data in TABLE I. Based on the MD values for HC_1, HC_2, and HC_3 (3.13, 2.96, and 4.02), one can classify this testing data to HC_2 because of the shortest MD. More details about the calculation of the MD and classification is explained in [26].

TABLE I
TRAINING DATA FOR EACH HEALTH CONDITION

Health condition	Sensor A	Sensor B
HC_1	$N(1.1,0.6^2)$	$N(1.5,0.4^2)$
HC_2	$N(1.7,0.5^2)$	$N(2.4,0.7^2)$
HC_3	$N(3.2,1.2^2)$	$N(5.1,0.9^2)$

TABLE II
TRAINING DATA FOR EACH HEALTH CONDITION

	Testing data		Mahalanobis Distance			Classified HC
	S_A	S_B	HC_1	HC_2	HC_3	
T1	3.02	1.45	3.13	2.96	4.02	HC_2
T2	6.70	3.79	10.73	9.85	3.18	HC_3
T3	0.05	2.06	2.32	3.28	4.21	HC_1
T4	2.01	3.56	11.08	7.27	9.44	HC_2
T5	-1.45	-0.52	6.54	7.41	7.16	HC_1
T6	2.08	0.79	2.44	2.48	5.01	HC_1

IV. SYSTEM MODELING AND OPTIMIZATION

A. System modeling

In this section, a reliability-based design optimization (RBDO) framework is explained for the piezoelectric patch design for a smart sensing network capable of failure diagnosis in skin structures. Fig. 4 depicts the configuration of the rectangular plate (40 cm × 30 cm × 1.15 mm) with the rivet joints indexed as J_1~J_8. A harmonic force F = 10 N with a frequency of 17 Hz is applied at the center of the plate. The design problem is formulated to use the minimum PZT material (shown by green squares in Fig. 4) that satisfies the failure detection performance (i.e. probability of detection for the rivet joint failure). Eight different joint failure modes (or health conditions, HCs) are defined to describe the combination of three joints' damage (J_4, J_6, J_7) as shown in TABLE III. The base structure (aluminum steel plate) has a relatively large scale (373 g) than the PZT patches attached to it (around 3g). Knowing there is a negligible change of the resonant frequency of the plate, we assumed the fixed vibration frequency throughout the optimization.

A finite element analysis (FEA) model is developed using ANSYS and the sensor output voltages and powers are calculated depending on the size and location of the PZT patches. Each HC is represented by different boundary conditions – fixed boundary condition is used for a healthy rivet joint (no damage) whereas no boundary condition is applied for a damaged one. Two different examples of harmonic analysis are shown in Fig. 5 where the health conditions are different (HC_0 and HC_7) and all the other configurations are identical (harmonic force and the PZT patch design). It can be observed that two different HCs are distinguished by the different voltage levels of each PZT patches (especially the lower two patches in this figure).

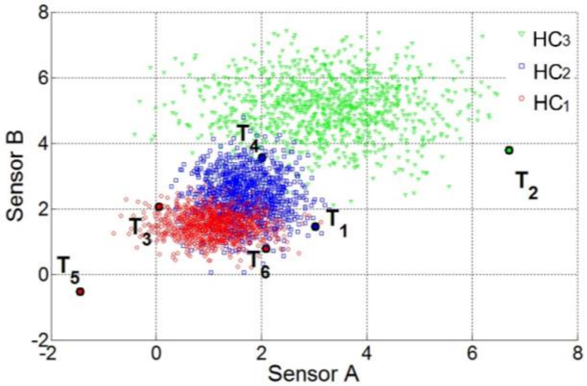

Fig. 3. Health condition classification using MD

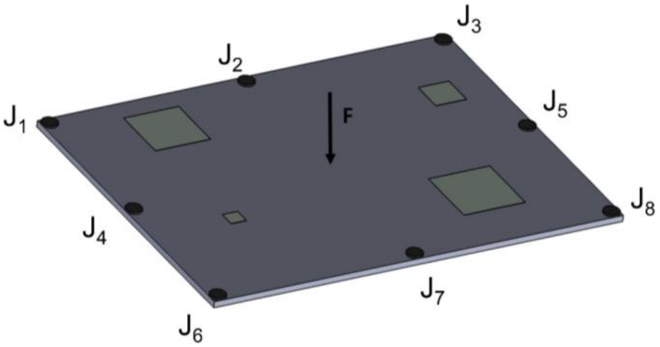

Fig. 4. Configuration of the skin plate with the attached rivet joints.

TABLE III
DEMONSTRATION OF DIFFERENT HC CATEGORIES

Health condition	Damaged joint	Health condition	Damaged joint
HC_0	N/A	HC_4	J_6, J_7
HC_1	J_6	HC_5	J_4, J_6
HC_2	J_7	HC_6	J_4, J_7
HC_3	J_4	HC_7	J_4, J_6, J_7

B. Reliability-based design optimization formulation

In this section, the sensor network design problem is formulated to find the location and size of the PZT patches that increase the distinction of the sensory data at each HC (detectability) while minimizing the use of PZT patches. Since there is uncertainty involved in the system such as loading condition and geometrical parameters, the sensory signal output is also uncertain. Reliability-based design optimization is conducted to consider the uncertainty of the system in the sensor network design process. RBDO is a methodology used in engineering design to find the best compromise between cost function and probabilistic constraints [31-32]. In this paper, the RBDO problem is formulated to minimize the total area of the sensor patches that satisfy the detectability target for each HC, or:

$$\begin{aligned} &Minimize && \sum_{j=1}^{N} A_j \\ &subject\,to: && D_i(\mathbf{x}, \boldsymbol{\theta}; \mathbf{d}) \geq D_T \\ & && \mathbf{x}^L \leq \mathbf{x} \leq \mathbf{x}^U \\ & && \mathbf{d}^L \leq \mathbf{d} \leq \mathbf{d}^U \end{aligned} \tag{11}$$

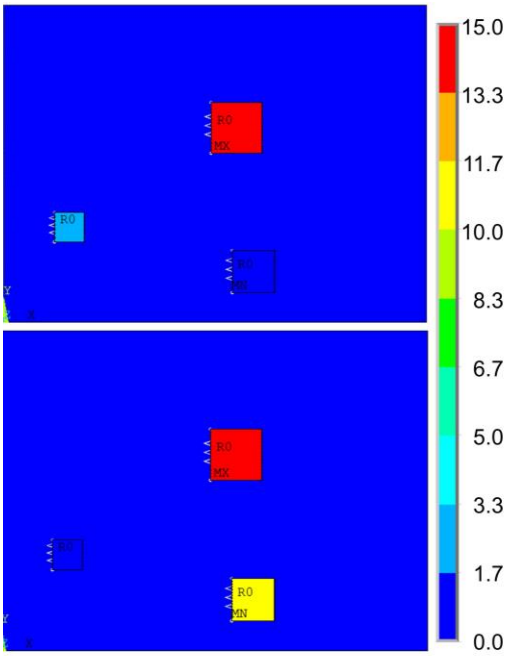

Fig. 5. Obtained simulated voltage (V) for different size and location of sensor patches (a) HC_0, (b) HC_7.

TABLE IV
RANDOM PARAMETERS FOR THE SENSOR NETWORK DESIGN

Random parameter	Description	Distribution type	Mean	Standard deviation
θ_1 (cm)	Length of plate	Normal	40	0.4
θ_2 (cm)	Width of plate	Normal	30	0.3
θ_3 (cm)	Force amplitude	Normal	10	0.1

TABLE V
DETERMINISTIC DESIGN VARIABLES FOR THE SENSOR NETWORK DESIGN

Variable	Description	Lower bound	Upper bound
X*j* (cm)	X coordinate of the *j*th sensor patch	0	34
Y*j* (cm)	Y coordinate of the *j*th sensor patch	0	24
S*j* (cm)	Side length of the *j*th sensor patch	2	6

A_j in the objective function represents the area for *j*th PZT square patch and *N* is the number of sensor patches that could vary from 1 to 4. Unlike usual energy harvester design problems, the power is not a performance measure to be maximized. Instead, the formulation considers the detectability that results in the difference of the harvested power from each piezoelectric patch. This formulation considers three random parameters ($\boldsymbol{\theta}$) that include the overall length, width of the plate, and the amplitude of harmonic force applied to the center of the plate. The deterministic design variable set ($\mathbf{d}$) comprises the side length of each squared PZT patch and its location – the X-Y coordinates of the left-bottom corner. In total there are 3 random parameters and 3×*N* number of design variables as depicted in TABLE IV and TABLE V, respectively.

The probabilistic detectability D_i in Eq. (3) is quantified in the form of a probability-of-detection (PoD) matrix to satisfy the detectability target D_T=99.5% [12]. The PoD matrix defines the probability of the correct detection for each predefined HC, and it indicates diagnostics ability of a failure detection system. A general form of PoD matrix is written as explained in Section II (equation (1)). The off-diagonal terms in the PoD indicate detection errors and the PoD = I (identity matrix) means the perfect failure detection.

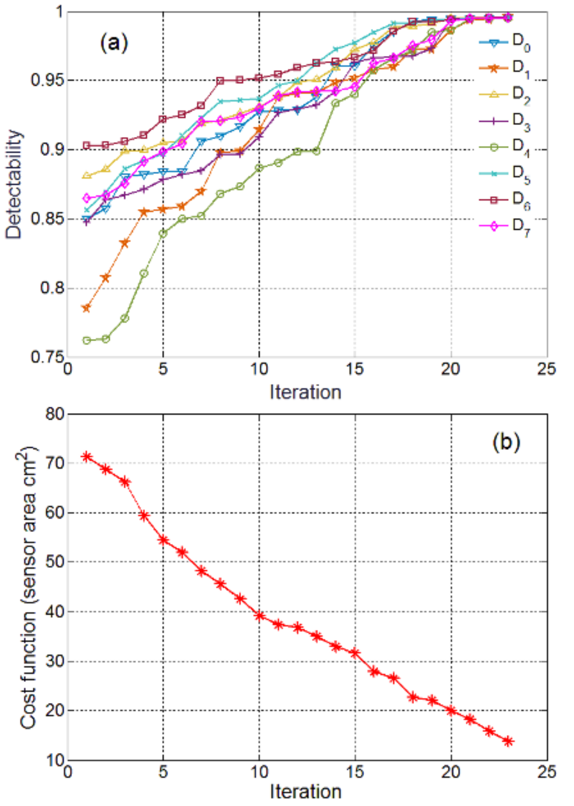

Fig. 6. RBDO iterative results (a) Detectability improvement; (b) Cost function reduction.

C. Sensor network design result

The genetic algorithm (GA) is adopted to search for the minimum sizes and optimum locations of multiple sensors that satisfy the detectability target. Four different optimization studies have been conducted by changing the number of PZT

This article has been accepted for publication in a future issue of this journal, but has not been fully edited. Content may change prior to final publication. Citation information: DOI 10.1109/TMECH.2020.3037291, IEEE/ASME Transactions on Mechatronics

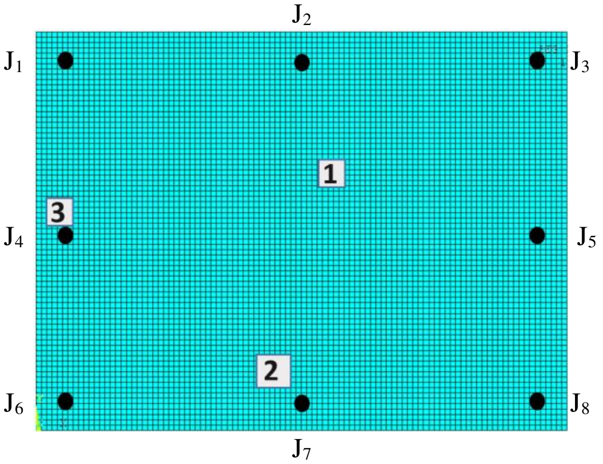

Fig. 7. Optimum location of the sensor patches.

sensors from N=1 to 4. The optimum solution is obtained for three sensor patches after 23 generations. The detectability variation can be reviewed graphically in Fig. 6(a). Throughout this optimization, the total area of the sensor patches has reduced from 71.36 to 13.76 cm^2 (Fig. 6(b)). The optimization history is presented in TABLE VI, and the optimal sensor locations are graphically shown in Fig. 7. The patch sizes are found as: 2.0^2 cm^2, 2.4^2 cm^2, and 2.0^2 cm^2. One can find that the final iteration satisfies the detectability constraints are larger than its target value (D_T =99.5%) for all of the eight health conditions.

D. *Experimental verification*

This section experimentally verifies the simulation-based optimization results in Section IV.C. The overall experimental setup for the design result is summarized in Fig. 8.

The PZT material (PSI -5A4E, Piezo Systems, USA) is cut to the size as found in the optimization study and attached on the plate using conductive epoxy. The aluminum plate is painted to eliminate electrical interaction with the sensors. Screw joints are used due to their convenience on health condition change (by fastening/loosening). A tightly fastened screw indicates the healthy condition and a loosened one represents the failed joint. The plate is excited by the electrodynamic shaker (ET-126B, Labworks Inc) at the center. The function generator (AFG3022C, Tektronix) is used to generate the electrical waveform for the harmonic excitation (10 N harmonic force at 17 Hz). The output voltage of each sensor is obtained using the oscilloscope (DS1054, RIGOL).

TABLE VI
ITERATIVE HISTORY OF RBDO FOR THE PLATE EXAMPLE (IN CM)

	X_1	Y_1	S_1	X_2	Y_2	S_2	X_3	Y_3	S_3
1	23.2	20	2	19.6	7.2	5.6	0	16	6
2	23.2	19.6	2.4	19.6	6.8	5.2	0	16	6
3	6	0.8	2.8	16.4	0.8	5.2	4.8	10.4	5.6
4	7.6	13.6	4.4	14.8	0.4	5.2	18	10.4	3.6
5	4	10.8	5.6	15.6	0	3.6	16.8	10	3.2
6	18.8	18.8	4	17.2	0.8	4.8	0	14.8	3.6
7	19.6	18.8	4	17.6	0.8	4.4	0	15.6	3.6
8	20	19.2	4	17.2	0.8	4.4	0	15.2	3.2
9	20	19.2	3.6	17.6	0.8	4.4	0	15.6	3.2
10	20	18.8	3.6	18	0.4	4	0	15.6	3.2
11	20	19.2	3.2	17.6	0.8	4.4	0	15.6	2.8
12	19.6	14.8	3.6	16.8	0.4	4	0	15.6	2.8
13	20	19.2	2.8	17.6	0.8	4.4	0	16	2.8
14	20	19.2	2.4	17.6	0.8	4.4	0	15.6	2.8
15	20.4	19.2	2.8	17.6	0.4	4	0	15.6	2.8
16	20.4	17.2	2	17.2	0.8	4	0	16	2.8
17	20.4	19.2	2.8	17.2	0.4	3.6	0	15.6	2.4
18	20.4	19.2	2.4	17.6	0.4	3.6	0	16	2
19	20.4	20	2	16	0.4	3.2	0	15.6	2.8
20	20.4	19.2	2.4	17.2	2.4	3.2	0	15.6	2
21	20.8	19.2	2	17.2	2.8	3.2	0	15.6	2
22	20.8	19.2	2	17.2	2.4	2.8	0	15.6	2
23	20.8	18.8	**2**	16.8	4	**2.4**	0	15.6	**2**

The average output power of PZT sensors with 8 health conditions is compared between the simulation and experiment as shown in Fig. 9. The output power of three sensors is measured at optimal resistive loads: 470 kΩ for sensor 1 and sensor 3; and 330 kΩ for sensor 2. The test result shows that Sensor 2 (close to J$_7$, see Fig. 7) produces power about two times large than simulation for HC$_5$. This condition refers to the health condition where J$_4$ and J$_6$ are loosened (left-middle and left-bottom), and it possibly increases strain level around J$_7$ (center-bottom) and makes Sensor 2 response very sensitive to the condition of J$_7$. However, we confirmed the overall agreement between the simulation and the experiment.

TABLE VII
DETERMINISTIC DESIGN VARIABLES FOR THE SENSOR NETWORK DESIGN

Component	Part number	Note
Rectifier	BAS3007	VF=0.35V at 100 mA
SPDT switch U1	TS5A3160	Rds-on=1Ω
Comparator U2	LTC1540	Iq= 0.3 μA
Transmitter U3	XBEE S2C	Vsupply = 2.1-3.6V

V. SYSTEM INTEGRATION

This section explains the details on power management circuit (PMC) design and system integration for self-powered wireless transmission.

A. *Overview on power management circuit*

This section presents the power management circuit (PMC) design as shown in Fig. 10, for a self-powered failure detection system. The components used in the proposed circuit are presented in TABLE VII. The proposed circuit consists of a full-bridge rectifier, a Single Pole Double Throw (SPDT) switch, a comparator with hysteresis, and a transmitter (Zigbee). A full-bridge rectifier converts the ac voltage to the dc voltage. The SPDT switch has low R$_{\text{ds-on}}$ and it efficiently

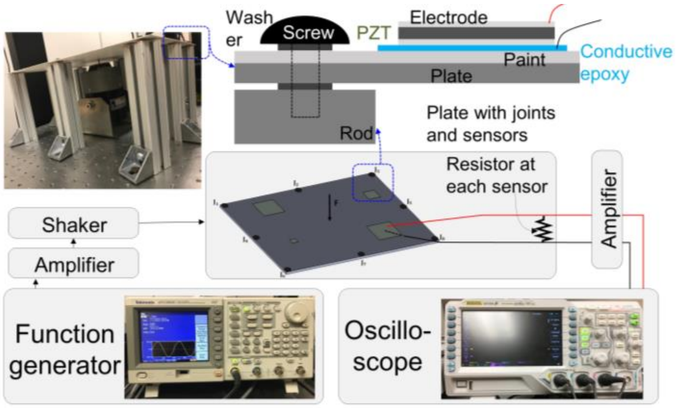

Fig. 8. Experimental setup for verification.

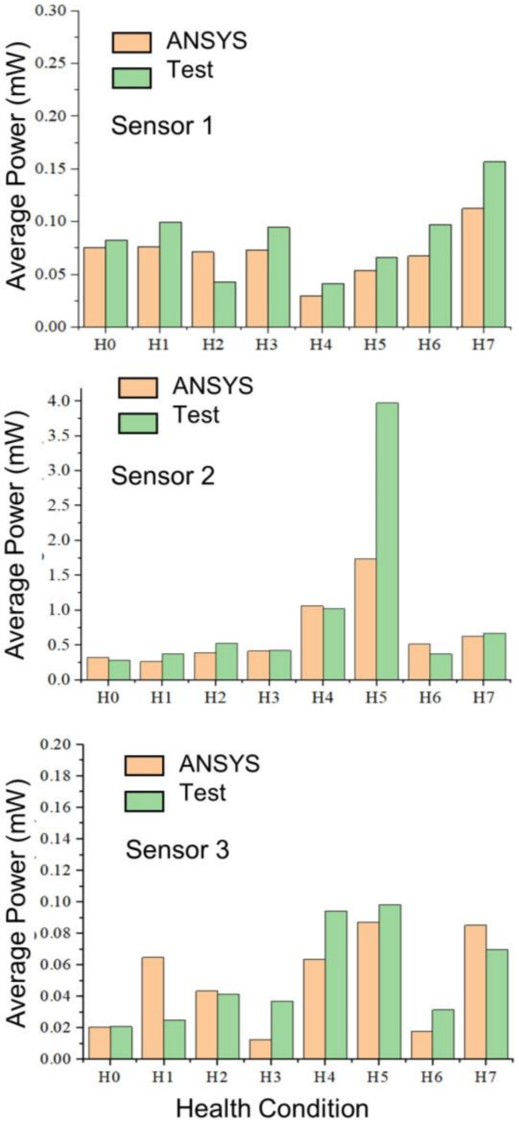

Fig. 9. Comparison results of health condition between simulation and test (a) sensor 1, (b) sensor 2, (c) sensor 3.

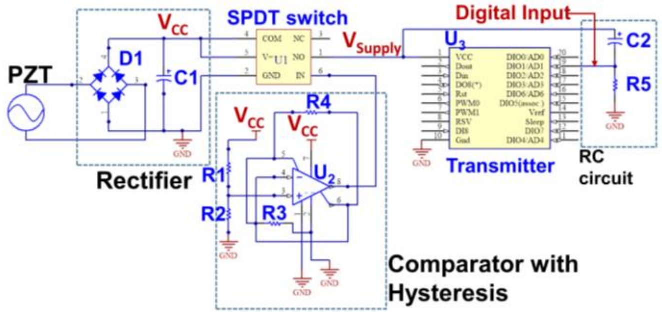

Fig. 10. Proposed circuit and wireless transmitter.

switches small scale of power supply (micro- to milli-watt) with low operating voltage (> 1.5 V) [33-34]. The comparator with hysteresis is used to control the SPDT switch. Zigbee communication module is selected for wireless transmission due to its lower power consumption than Wifi and CDMA and longer transmission range than Bluetooth.

B. SPDT switch and comparator with hysteresis

In the proposed sensor node, a SPDT switch and comparator with hysteresis is proposed to accumulate the microwatt scale of power from the PZT and supply it to the wireless transmitter. The working principle is explained in Fig. 11. The SPDT switch turns off during the charging period of the capacitor (C1 in Fig. 10). When the capacitor voltage (Vcc in Fig. 10) reaches to the upper level of threshold voltage ("Turn on" in Fig. 11), the comparator sends the HIGH signal (Power supply "On" in Fig. 11) to turn on the SPDT switch and then the stored energy in C1 is transferred to wireless transmitter U3 ("Data Transmission" in Fig. 11). While the SPDT switch turns on, C1 is discharged and Vcc decreases. When Vcc reaches to the low level of threshold voltage ("Turn off" in Fig. 11), the comparator sends LOW to SPDT switch to turn off. This process is repeated the entire cycle for powering the wireless transmitter using low power from the PZT patch. When the power level from the PZT is changed due to the change of health condition, the transmission rate changes accordingly as shown in Fig. 11.

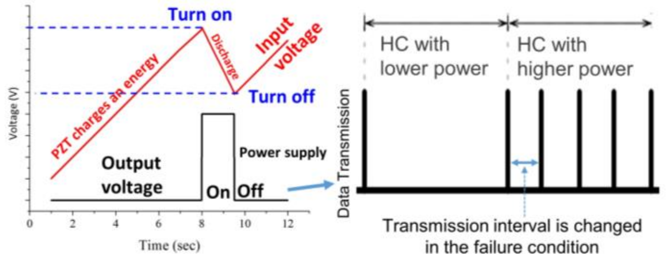

Fig. 11. Working principle of SPDT switch and comparator with hysteresis.

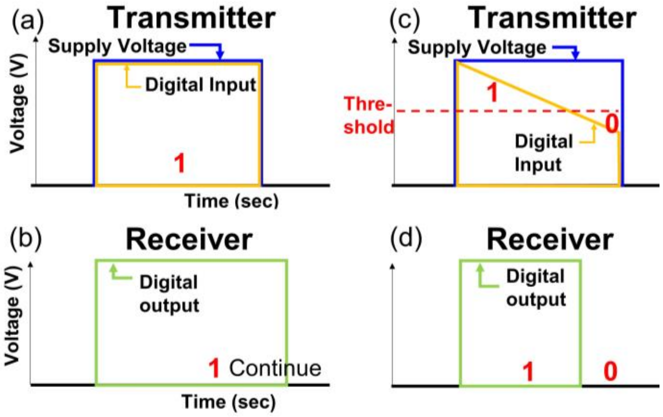

Fig. 12. Supply voltage and digital signal of (a) transmitter without RC circuit, (b) receiver without RC circuit, supply voltage and digital signal of (c) transmitter with RC circuit, (d) receiver with RC circuit.

C. RC circuit for reliable wireless signal transmission

This section presents the RC circuit for transmitting the digital signal. The digital input to the transmitter is sourced from the supply voltage (V_{supply}) through the RC circuit (Fig. 10). The RC circuit is required to successfully transmit the HIGH and LOW signals from a transmitter to a receiver in every cycle.

Fig. 12 explains the problem when there is no RC circuit (Fig. 12(a), (b)) and how the RC circuit resolves it (Fig. 12(c), (d)). In both cases, when the transmitter has the supply voltage and the digital input at HIGH (=1) as shown in Fig. 12(a), (c), the Zigbee receiver generates the corresponding digital signal (HIGH=1) after start-up time (Fig. 12(b), (d)). This digital output should go LOW when the digital input in the transmitter goes LOW (=0). If there is no RC circuit, however, the supply voltage and the digital input go LOW simultaneously and there is no lead time for the receiver to detect the digital input change from HIGH to LOW. To solve this problem, the transmitter needs to stay turned on (supply voltage = HIGH) even after the digital input goes LOW (below the threshold) as shown in Fig 10(c). Then the change of digital input is successfully transmitted to the receiver. The output voltage of the RC circuit is reduced based on the RC time constant (τ=RC=R_5C_2 in Fig. 10).

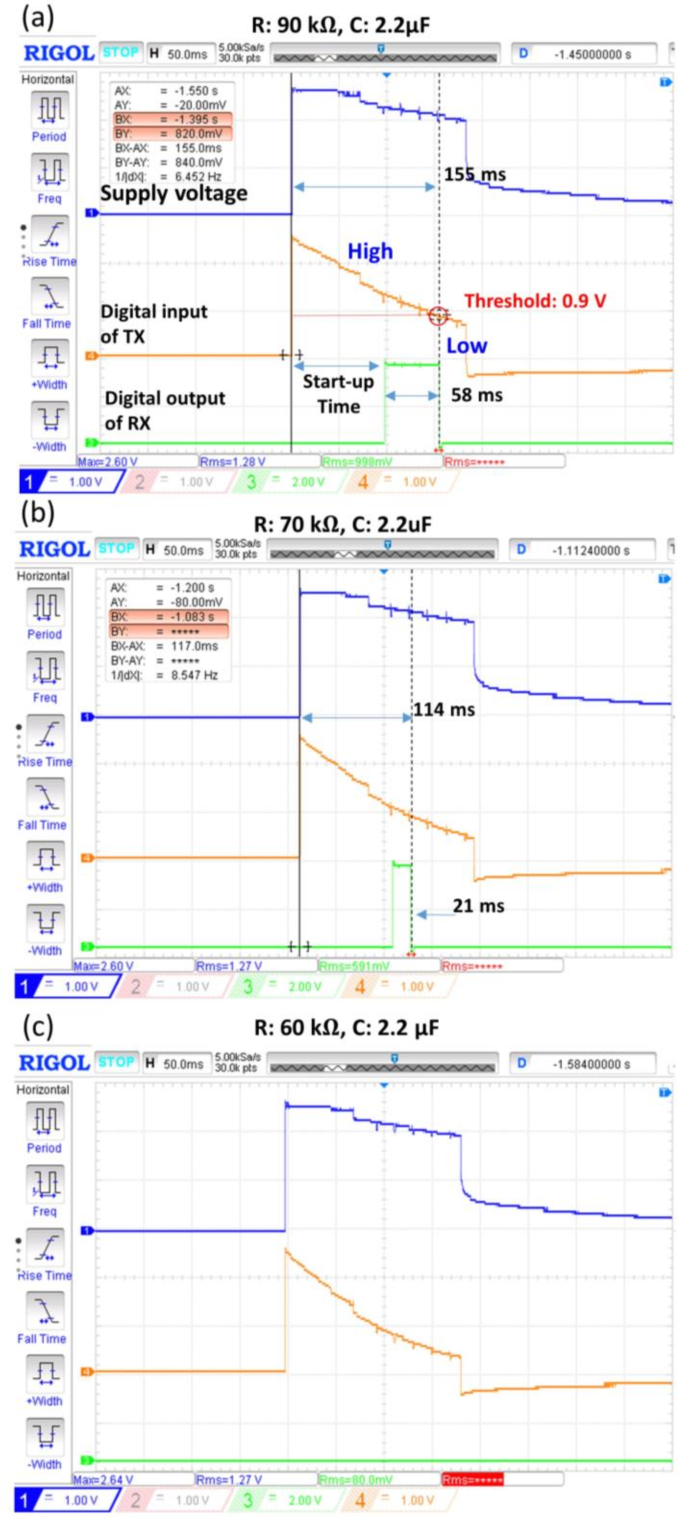

Fig. 13. Test results with supply voltage, digital input of transmitter, and digital output of receiver with the different RC values.

Fig. 13(a) shows the test results with the supply voltage, the RC circuit output that is the digital input to the transmitter, and the digital output of the receiver. When the supply voltage (blue line) turns on, the digital input to the transmitter (orange line) rises rapidly and decreases gradually to reach LOW (threshold voltage = 0.9V) before the supply voltage goes LOW. The digital output in the receiver (green line) turns on after start-up time and goes LOW (0) when the digital input to the transmitter becomes LOW. This test result shows that the digital input signal with the RC circuit is successfully transmitted to the receiver.

Each transmission time duration needs to be minimized to reduce the power consumption of the transmitter and increase the resolution of detection. We performed the parameter study on RC values to minimize the transmission time as shown in Fig. 13. As measured in Fig. 13, the capacitance discharges more rapidly when the RC time constant (τ=RC) is reduced. For example, digital signal transmission takes 155 ms when R=90 kΩ and C=2.2 µF (Fig. 13(a)), and it reduces down to 114 ms when R=70 kΩ and C=2.2 µF (Fig. 13(b)). When R is further reduced (60 kΩ), the receiver cannot detect the change of the digital signal because the digital input becomes LOW (0) before the start-up is finished. This paper selects the case in Fig. 13(b) with R(=R_5)=70 kΩ, C(=C_2)=2.2 µF, transmission time = 114 ms, and ON time of the receiver = 21 ms.

D. *Selection of charging capacitor*

The charging capacitor C_1 (see Fig. 10) is selected to supply sufficient power to the wireless transmitter, based on the dissipated energy E_d as Eq. (12).

$$E_d = E_1 - E_2 = 0.5C_1V_{CC\_1}^2 - 0.5C_1V_{CC\_2}^2 \tag{12}$$

where E_1 and E_2 are the stored energy in the capacitor before and after discharge, and V_{CC_1} and V_{CC_2} are the capacitor voltage before and after discharge, respectively. The dissipated energy in the capacitor E_d should be higher than the required energy per transmission (3.93 mJ) based on the average supply

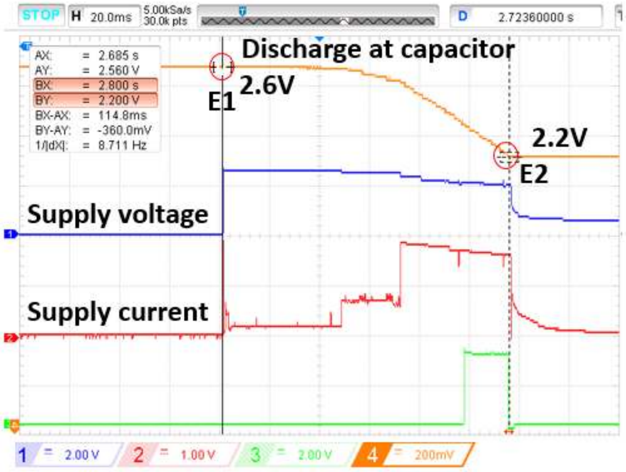

Fig. 14. The output voltage of capacitor C1, supply voltage of transmitter, supply current, and digital output of receiver.

current (15 mA) and voltage of transmitter (2.3 V).

Given the difference between V_{CC_1} and V_{CC_2} (0.4 V) limited by the comparator specification [35], V_{CC_2} and is set to 2.2 V (minimum operation voltage of wireless transmitter) and V_{CC_1} is set to 2.6 V to minimize the power consumption of wireless transmitter. The capacitance value is set as C_1 = 4.7 mF that supplies the power (4.20 mJ per transmission) larger than 3.93 mJ. Fig. 14 show the experimental study on the output voltage of capacitor C_1 (orange), the supply voltage of transmitter (blue), the supply current (red), and the digital output of the receiver (green line). When capacitor C_1 discharges energy by the voltage drop from 2.6 V to 2.2 V, this energy successfully transmits the signal for 144 ms and the receiver also generates the digital output signal.

VI. SYSTEM FEASIBILITY TEST ON JOINT FAILURE DETECTION

The proposed self-powered failure monitoring system is tested for evaluating the detectability of the system as shown in Fig. 15. Each PZT sensor is connected to the proposed circuit and the wireless transmitter to detect the failure of the joints. Wireless transmission is tested with a relatively long distance (30 m) and the average transmission rate (number of transmissions per minute) is obtained by taking an average of three (3) transmission intervals.

TABLEs VIII to X and Fig. 16 shows the transmission rate from each sensor node at different health conditions. For example, if the transmission rate (number of transmissions per minute) of sensor 1, 2, and 3 are close to (0.5, 8.8, 0.9), it corresponds to health condition HC_5 (Joint 4 and 6 are failed). More systematically, HC can be identified using the Mahalanobis distance (MD) to each health condition data (equation (10)) and the health condition can be identified by the minimum MD. When the transmission rate is (0.5, 8.8, 0.9), the MD to HC_5 is measured as 2.718 which is minimum among others. The next smallest MD is to HC_4 (112.816), followed by very large MDs for the other HCs. So, this transmission rate corresponds to HC_5.

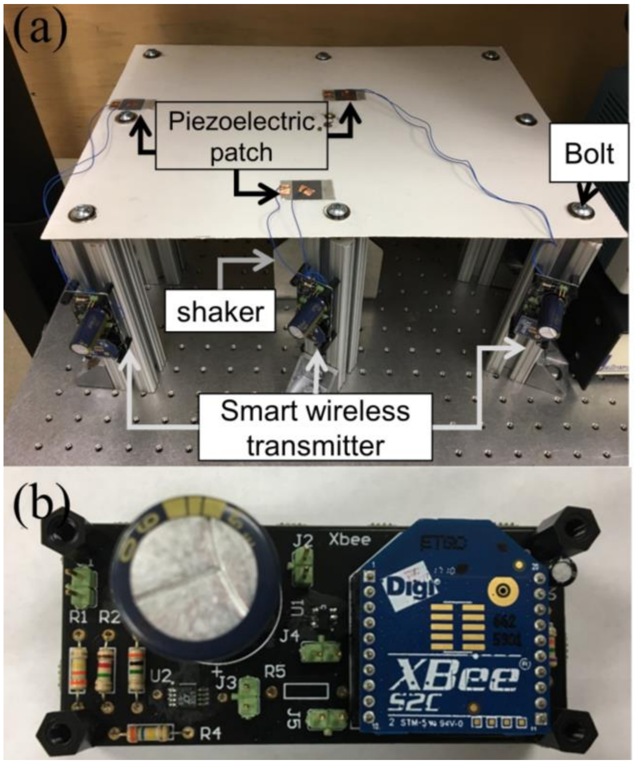

Fig. 15. (a) Test setup with proposed circuit and wireless transmitter (b) proposed circuit and wireless transmitter.

From the numerical data in the tables, one can find that the transmission rate is very consistent from three trials. Besides, the proportional relationship between voltage, power, and transmission rate is found from all of the health conditions. The sensor network design by RBDO makes it possible to have clearly distinguished transmission rates even with the uncertainty. In most cases, the transmission rate from sensor 2 is higher than sensor 1 and sensor 3 due to its higher average output power than the other sensors as reviewed in Fig. 9. To summarize, the proposed self-powered failure detection method can detect multiple joint failure modes (or health conditions) by different transmission rates from multiple wireless sensor nodes

TABLE VIII
VOLTAGE, POWER, AND TRANSMISSION RATE OF SENSOR 1 AT DIFFERENT HEALTH CONDITIONS

Health condition	RMS Voltage (V)	Average Power (µW)	Transmission rate (number of trans / min)			
			Trial 1	Trial 2	Trial 3	Average
HC0	6.22	82.32	0.433	0.434	0.433	0.433
HC1	6.83	99.25	0.573	0.576	0.575	0.574
HC2	4.48	42.70	0.289	0.284	0.277	0.283
HC3	6.66	94.37	0.465	0.467	0.456	0.462
HC4	4.41	41.38	0.362	0.367	0.364	0.364
HC5	5.58	66.25	0.488	0.497	0.495	0.493
HC6	6.75	96.94	0.569	0.570	0.563	0.567
HC7	8.58	156.63	1.087	1.091	1.038	1.071

TABLE IX
VOLTAGE, POWER, AND TRANSMISSION RATE OF SENSOR 2 AT DIFFERENT HEALTH CONDITIONS

Health condition	RMS Voltage (V)	Average Power (µW)	Transmission rate (number of trans / min)			
			Trial 1	Trial 2	Trial 3	Average
HC0	9.69	280.45	1.210	1.217	1.222	1.216
HC1	11.1	373.36	1.399	1.399	1.376	1.391
HC2	13.2	528.00	1.753	1.741	1.726	1.740
HC3	11.8	421.93	1.480	1.491	1.529	1.500
HC4	18.4	1025.9	3.049	3.061	3.057	3.056
HC5	36.2	3971.0	8.535	9.288	8.746	8.856
HC6	11.1	373.36	1.336	1.333	1.337	1.335
HC7	14.9	672.75	2.336	2.333	2.356	2.342

TABLE X
VOLTAGE, POWER, AND TRANSMISSION RATE OF SENSOR 3 AT DIFFERENT HEALTH CONDITIONS

Health condition	RMS Voltage (V)	Average Power (µW)	Transmission rate (number of trans / min)			
			Trial 1	Trial 2	Trial 3	Average
HC0	3.13	20.84	0.060	0.061	0.061	0.061
HC1	3.43	25.03	0.086	0.084	0.086	0.085
HC2	4.40	41.19	0.211	0.210	0.211	0.211
HC3	4.17	36.99	0.122	0.120	0.120	0.121
HC4	6.66	94.37	0.458	0.436	0.429	0.441
HC5	6.80	98.38	0.867	0.871	0.874	0.870
HC6	3.84	31.37	0.119	0.120	0.120	0.119
HC7	5.73	69.85	0.916	0.904	0.923	0.914

This article has been accepted for publication in a future issue of this journal, but has not been fully edited. Content may change prior to final publication. Citation information: DOI 10.1109/TMECH.2020.3037291, IEEE/ASME Transactions on Mechatronics

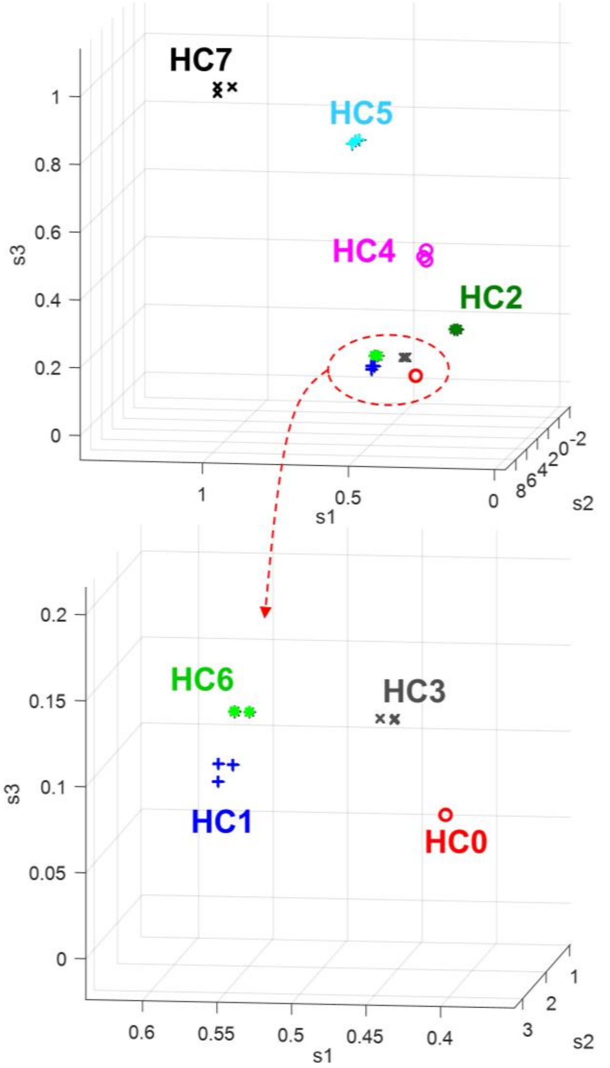

Fig. 16. Transmission per minute of sensor, and distributions of for different health condition.

using extremely low power.

VII. Conclusion

This paper presents a self-powered wireless failure detection method that monitors the joint status using wireless transmission rates from multiple harvesters. The proposed detection method uses the energy harvesting function of PZT material, and the power management circuit (PMC) is designed to supply power to the wireless transmitter. First, we performed a reliability-based design optimization of wireless sensor network that determines the size and location of multiple PZT patches for joint failure detection using the detectability measure. Second, we designed the power management circuit – consisting of a full-bridge rectifier, a Single Pole Double Throw (SPDT) switch, a comparator with hysteresis – that acquires microwatt scale power from each PZT and supplies it continuously to the Zigbee wireless transmitter. Experimental results show that all of the health conditions are well distinguished with the different transmission rates.

The advantages of the proposed sensor node are: (1) a simple layout composed of PZT sensor, wireless transmitter, and PMC; (2) dramatically reduced power consumption of wireless transmitter due to milliseconds of transmission time and extremely low sampling frequency; and (3) extended number of charge/discharge cycles (e.g. 1 million ~) using a small capacity of the capacitor (1~10 mF). We envision the proposed sensor node can be implemented as a part of the skin structure so that it can autonomously detect its structural defects. The future study includes a realistic engineering monitoring such as a railroad system (e.g. bogie) under steady velocity. Understanding the limitation of the current study to detect a discrete combination of known failure modes under fixed frequency vibration, the method needs an update to detect unknown failure modes and consider random vibration loading.

References

[1] Song, G., Li, H., Gajic, B., Zhou, W., Chen, P., & Gu, H. (2013). Wind turbine blade health monitoring with piezoceramic-based wireless sensor network. International Journal of Smart and Nano Materials, 4(3), 150-166.

[2] Giurgiutiu, V. (2005). Tuned Lamb wave excitation and detection with piezoelectric wafer active sensors for structural health monitoring. Journal of intelligent material systems and structures, 16(4), 291-305.

[3] Giurgiutiu, V., Zagrai, A., & Bao, J. (2002). Piezoelectric wafer embedded active sensors for aging aircraft structural health monitoring. Structural Health Monitoring, 1(1), 41-61.

[4] Gupta, V., Sharma, M., & Thakur, N. (2010). Optimization criteria for optimal placement of piezoelectric sensors and actuators on a smart structure. Journal of Intelligent Material Systems and Structures, 21(12), 1227-1243.

[5] Singhal, N., Sharma, M., & Mangal, S. K. (2017). Optimal placement of piezoelectric patches over a smart structure. Integrated Ferroelectrics, 183(1), 60-90.

[6] Lee, A., and Chen, S., 1994, "Collocated sensor/actuator positioning and feedback design in the control of flexible structure system," ASME, J. Vib. Acoust, pp. 146–154.

[7] Cha, Y. J., Agrawal, A. K., Kim, Y., & Raich, A. M. (2012). Multi-objective genetic algorithms for cost-effective distributions of actuators and sensors in large structures. Expert Systems with Applications, 39(9), 7822-7833.

[8] Chhabra, D., Bhushan, G., & Chandna, P. (2016). Optimal placement of piezoelectric actuators on plate structures for active vibration control via modified control matrix and singular value decomposition approach using modified heuristic genetic algorithm. Mechanics of advanced materials and structures, 23(3), 272-280.

[9] Guratzsch, R. F., & Mahadevan, S. (2010). Structural health monitoring sensor placement optimization under uncertainty. AIAA journal, 48(7), 1281-1289.

[10] Castro-Triguero, R., Murugan, S., Gallego, R., & Friswell, M. I. (2013). Robustness of optimal sensor placement under parametric uncertainty. Mechanical Systems and Signal Processing, 41(1-2), 268-287.

[11] Vincenzi, L., & Simonini, L. (2017). Influence of model errors in optimal sensor placement. Journal of Sound and Vibration, 389, 119-133.

[12] Wang, P., Wang, Z., Youn, B. D., & Lee, S. (2015). Reliability-based robust design of smart sensing systems for

failure diagnostics using piezoelectric materials. Computers & Structures, 156, 110-121.

[13] O'Donnell, C., Palacin, R., & Rosinski, J. (2006). Pantograph damage and wear monitoring system, pp. 178–181.

[14] Chebrolu, K., Raman, B., Mishra, N., Valiveti, P. K., & Kumar, R. (2008, June). Brimon: a sensor network system for railway bridge monitoring. In Proceedings of the 6th international conference on Mobile systems, applications, and services (pp. 2-14).

[15] Nelson, C. A., Platt, S. R., Albrecht, D., Kamarajugadda, V., & Fateh, M. (2008,). Power harvesting for railroad track health monitoring using piezoelectric and inductive devices. In Active and Passive Smart Structures and Integrated Systems 2008 (Vol. 6928, p. 69280R). International Society for Optics and Photonics.

[16] Nechibvute, A., Chawanda, A., & Luhanga, P. (2012). Piezoelectric energy harvesting devices: an alternative energy source for wireless sensors. Smart Materials Research, 2012.

[17] Tan, H. P., Lee, P. W., Seah, W. K., & Eu, Z. A. (2009, May). Impact of power control in wireless sensor networks powered by ambient energy harvesting (WSN-HEAP) for railroad health monitoring. In 2009 International Conference on Advanced Information Networking and Applications Workshops (pp. 804-809). IEEE.

[18] Arms, S. W., Townsend, C. P., Churchill, D. L., Galbreath, J. H., & Mundell, S. W. (2005, May). Power management for energy harvesting wireless sensors. In Smart Structures and Materials 2005: Smart Electronics, MEMS, BioMEMS, and Nanotechnology (Vol. 5763, pp. 267-275). International Society for Optics and Photonics.

[19] Park, G., Rosing, T., Todd, M. D., Farrar, C. R., & Hodgkiss, W. (2008). Energy harvesting for structural health monitoring sensor networks. Journal of Infrastructure Systems, 14(1), 64-79.

[20] Maruccio, C., Quaranta, G., De Lorenzis, L., & Monti, G. (2016). Energy harvesting from electrospun piezoelectric nanofibers for structural health monitoring of a cable-stayed bridge. Smart Materials and Structures, 25(8), 085040.

[21] Esu, O. O., Lloyd, S. D., Flint, J. A., & Watson, S. J. (2016). Feasibility of a fully autonomous wireless monitoring system for a wind turbine blade. Renewable Energy, 97, 89-96.

[22] Elahi, H., Eugeni, M., & Gaudenzi, P. (2018). A review on mechanisms for piezoelectric-based energy harvesters. Energies, 11(7), 1850.

[23] Lim, D. W., Mantell, S. C., & Seiler, P. J. (2017). Wireless monitoring algorithm for wind turbine blades using Piezo-electric energy harvesters. Wind Energy, 20(3), 551-565.

[24] Chew, Z. J., Ruan, T., Zhu, M., Bafleur, M., & Dilhac, J. M. (2017). Single piezoelectric transducer as strain sensor and energy harvester using time-multiplexing operation. IEEE Transactions on Industrial Electronics, 64(12), 9646-9656.

[25] Wang, P., Youn, B. D., Hu, C., Ha, J. M., & Jeon, B. (2015). A probabilistic detectability-based sensor network design method for system health monitoring and prognostics. Journal of Intelligent Material Systems and Structures, 26(9), 1079-1090.

[26] Eshghi, A. T., Lee, S., Jung, H., & Wang, P. (2019). Design of structural monitoring sensor network using surrogate modeling of stochastic sensor signal. Mechanical Systems and Signal Processing, 133, 106280.

[27] Nguyen, T., Chan, T. H., & Thambiratnam, D. P. (2014). Controlled Monte Carlo data generation for statistical damage identification employing Mahalanobis squared distance. Structural Health Monitoring, 13(4), 461-472.

[28] Nguyen, T., Chan, T. H., & Thambiratnam, D. P. (2014). Field validation of controlled Monte Carlo data generation for statistical damage identification employing Mahalanobis squared distance. Structural Health Monitoring, 13(4), 473-488.

[29] Mosavi, A., Dickey, D., Seracino, R. (2012). Identifying damage locations under ambient vibrations utilizing vector autoregressive models and Mahalanobis distances. Mechanical systems and signal processing, 26, 254-267.

[30] Kim, Y., Chong, J. W., Chon, K. H., & Kim, J. (2012). Wavelet-based AR–SVM for health monitoring of smart structures. Smart Materials and Structures, 22(1), 015003.

[31] Eshghi, A. T., & Lee, S. (2019). Adaptive improved response surface method for reliability-based design optimization. Engineering Optimization, 51(12), 2011-2029.

[32] Eshghi, A. T., Lee, S., Sadoughi, M. K., Hu, C., Kim, Y. C., & Seo, J. H. (2017). Design optimization under uncertainty and speed variability for a piezoelectric energy harvester powering a tire pressure monitoring sensor. Smart Materials and Structures, 26(10), 105037.

[33] Texas Instruments, TS4A3160 SPDT Analog Switch, 2017 (https://www.ti.com/lit/ds/symlink/ts5a3160.pdf).

[34] NXP, Low power, low ohmic switches for analog and digital switching, 2017, (https://www.nxp.com/docs/en/brochure/75017373.pdf).

[35] Linear Technology, LTC1540 Nanopower Comparator with Reference, 2017 (https://www.analog.com/en/products/ltc1540.html#product-overview, Last date of access: Jan. 2019).

Hyun Jun Jung received his Ph.D degree from the department of Electrical engineering in Hanyang University, Seoul, South Korea, in 2017. He was a postdoctoral researcher at the University of Maryland Baltimore County, Baltimore, USA, and currently he is a postdoctoral researcher at Virginia Tech. His research interest includes a low power management circuit, wireless sensor node, and piezoelectric energy harvesting device.

Amin Toghi Eshghi received his Ph.D. in mechanical engineering from University of Maryland, Baltimore County, MD, USA, in March 2019. He is currently a data scientist at Juniper Networks. His research interests include robust optimization, stochastic optimization, design under uncertainty, and machine learning applications in engineering optimization.

Soobum Lee received his Ph.D. degree from the department of Mechanical Engineering in KAIST, Korea, in 2007. He is currently he is an associate professor at the University of Maryland Baltimore County. His main research interests include energy harvesting device design, structural topology optimization, robust and reliability based design optimization.